

Coupling FEM with a multiple-subdomain Trefftz method

D. Casati and R. Hiptmair

Research Report No. 2019-45
September 2019

Seminar für Angewandte Mathematik
Eidgenössische Technische Hochschule
CH-8092 Zürich
Switzerland

Coupling FEM with a multiple-subdomain Trefftz method

Daniele Casati · Ralf Hiptmair

Abstract We consider 2D electromagnetic scattering at bounded objects consisting of different, possibly inhomogeneous materials. We propose and compare three approaches to couple the Finite Element Method (FEM) in a meshed domain encompassing material inhomogeneities and the Multiple Multipole Program (MMP) in the unbounded complement.

MMP is a Trefftz method, as it employs trial spaces composed of exact solutions of the homogeneous problem. Each of these global basis functions is anchored at a point that, if singular, is placed outside the respective domain of approximation.

In the MMP domain we assume that material parameters are piecewise constant, which induces a partition: one unbounded subdomain and other bounded, but possibly very large, subdomains, each requiring its own Trefftz trial space.

Coupling approaches arise from seeking stationary points of Lagrangian functionals that both enforce the variational form of the equations in the FEM domain and match the different trial functions across subdomain interfaces. Hence, on top of the transmission conditions connecting the FEM and MMP domains, one also has to impose transmission conditions between the MMP subdomains.

Specifically, we consider the following coupling approaches:

1. *Least-squares-based coupling* using techniques from PDE-constrained optimization.
2. *Multi-field variational formulation* in the spirit of mortar finite element methods.
3. *Discontinuous Galerkin coupling* between the meshed FEM domain and the single-entity MMP subdomains.

We compare these approaches in a series of numerical experiments with different geometries and material parameters, including examples that exhibit triple-point singularities.

Keywords Finite Element Method · Trefftz method · Method of Auxiliary Sources · Multiple Multipole Program · wave scattering

Mathematics Subject Classification (2010) MSC 35Q61 · MSC 65N30 · MSC 65N80 · MSC 65Z05

This work was supported by the Swiss National Science Foundation [grant number 2000021_165674/1].

D. Casati

Seminar for Applied Mathematics, ETH Zurich, Rämistrasse 101, 8092 Zurich, Switzerland

Tel.: +41-44-6323112

Fax: +41-44-6321104

E-mail: daniele.casati@sam.math.ethz.ch

R. Hiptmair

Seminar for Applied Mathematics, ETH Zurich, Rämistrasse 101, 8092 Zurich, Switzerland

1 Introduction

We consider the following second-order scalar elliptic boundary value problem:

$$-\nabla \cdot [\mathbf{M}_\epsilon^{-1}(\mathbf{x}) \nabla u] - \omega^2 \mu(\mathbf{x})u = f \quad \text{in } \mathbb{R}^2, \quad (1a)$$

$$\nabla u \cdot \mathbf{x} - ik\|\mathbf{x}\|u = 0 \quad \text{for } \|\mathbf{x}\| \rightarrow \infty \text{ uniformly}, \quad (1b)$$

which models the scattering of transverse-electric polarized z -invariant time-harmonic electromagnetic waves at penetrable objects [16, p. 356, Section 8.2]. Here,

- $u : \mathbb{R}^2 \rightarrow \mathbb{C}$ represents the longitudinal component of the magnetic field (usually denoted as H_z in electromagnetism).
- $\mathbf{M}_\epsilon : \mathbb{R}^2 \rightarrow \mathbb{C}^{2,2}$ and $\mu : \mathbb{R}^2 \rightarrow \mathbb{C}$ are material parameters corresponding to an inhomogeneous, anisotropic *permittivity* (\mathbf{M}_ϵ with nonzero determinant) and an inhomogeneous, isotropic *permeability*, respectively. Given a bounded domain $\Omega_\star \subset \mathbb{R}^2$, we assume that, in $\mathbb{R}^2 \setminus \Omega_\star$, $\mathbf{M}_\epsilon = \epsilon \mathbf{I}$ and ϵ, μ are *piecewise constant*.
- $\omega \in \mathbb{R}$ is the *angular frequency*, while $k := \omega\sqrt{\epsilon\mu}$ the piecewise-constant *wavenumber* in $\mathbb{R}^2 \setminus \Omega_\star$.
- $f : \mathbb{R}^2 \rightarrow \mathbb{R}$ represents the stationary current that generates the electromagnetic field. f has compact support in Ω_\star .
- (1b) is the *Sommerfeld radiation condition*; please refer to [9, p. 19, Definition 2.4].

Piecewise-constant ϵ, μ in $\mathbb{R}^2 \setminus \Omega_\star$ induce a natural partition of $\mathbb{R}^2 \setminus \Omega_\star$ into $m + 1$ subdomains Ω_i , $i = 0, \dots, m$, such that the pair $(\epsilon, \mu) \in \mathbb{C}^2$ (and therefore the wavenumber k) is constant in each Ω_i . We denote the constant wavenumber in each subdomain with k_i , $i = 0, \dots, m$, and assume that there is only one unbounded domain in this partition, which we refer to as Ω_0 .

To simplify the exposition and without loss of generality, from now on we assume that $m = 1$, i.e. that $\Omega_0 \cup \Omega_1 = \mathbb{R}^2 \setminus \Omega_\star$, with constant $k_0 \in \mathbb{C}$ in the unbounded domain Ω_0 and constant $k_1 \in \mathbb{C}$ in the bounded Ω_1 . Generalization to $m > 1$ is straightforward.

In Ω_0 , the weak solution $u \in H_{loc}^1(\mathbb{R}^2)$ of (1) belongs to the continuous *Trefftz space*¹

$$\mathcal{T}(\Omega_0) := \left\{ v \in H_{loc}^1(\Omega_0) : \nabla^2 v + k_0^2 v = 0, \text{ } v \text{ satisfies radiation condition (1b)} \right\}; \quad (2a)$$

in Ω_1 , u belongs to

$$\mathcal{T}(\Omega_1) := \left\{ v \in H^1(\Omega_1) : \nabla^2 v + k_1^2 v = 0 \right\}. \quad (2b)$$

Trefftz methods seek to approximate the unknown in $\mathbb{R}^2 \setminus \Omega_\star$ using some finite-dimensional subspace of $\mathcal{T}(\Omega_0), \mathcal{T}(\Omega_1)$. Our approach uses spaces spanned by multipole expansions centered in points outside each Ω_i , $i = 0, 1$, which is being approximated. We refer to this discretization as the MMP approximation after the Trefftz method known as *Multiple Multipole Program*; see Section 2 for details.

However, functions in Trefftz spaces cannot approximate the unknown in Ω_\star , where \mathbf{M}_ϵ, μ may vary in space. There we employ a standard *finite element space* to discretize the usual primal variational form of (1).

The main issue arising is how to impose the coupling between the domains of MMP and the domain of the *Finite Element Method* (FEM). Several algorithms are presented in Section 3 and their convergence is shown numerically in Section 4.

⁰ *Abbreviations.* MMP: Multiple Multipole Program. FEM: Finite Element Method. TPS: Triple-Point Singularity. PDE: Partial Differential Equation. DG: Discontinuous Galerkin. DoF: Degree of Freedom. BEM: Boundary Element Method. Subscript f in formulas: FEM. Subscript m in formulas: MMP. Superscript n in formulas: discrete.

¹ The subscript “loc” indicates that functions belong to the reported space after multiplication with a compactly-supported smooth function.

1.1 State of the Art

The coupling between FEM and MMP for the Poisson's equation in both 2D and 3D has been discussed by the authors from the perspective of numerical analysis in [7], while [8] illustrates numerical experiments for 3D Maxwell's equations (magnetostatics). The approaches we propose here to realize the coupling have been described in these works for the first time.

The FEM–MMP coupling has also been tackled before from an engineering perspective [24]. A different methodology for coupling FEM and MMP is used in that work: the authors match field values, the Dirichlet data, in selected points on the interface between the FEM and MMP domains (*collocation method*), while the Neumann data enter through a boundary term of the variational form. The resulting overdetermined FEM–MMP system of equations is solved in the least-squares sense.

To the best of our knowledge, apart from these papers little research has been devoted to the investigation of strategies combining Trefftz methods with conventional finite element methods.

The novelty of this work lies in using FEM with more than one MMP domain, which allows to treat piecewise-constant material parameters on potentially very large domains while keeping a minimal volume mesh for the FEM domain. This mesh can be so small that it only surrounds points where the solution is singular, like *Triple-Point Singularities* (TPS), which arise at the junction of three different materials [11]. At the same time, one also needs to impose transmission conditions between neighboring MMP domains, which requires a mesh on the interface separating them.

Another new aspect of this work is the application of the FEM–MMP coupling to scattering problems, for which low-order mesh-based methods like FEM suffer from the well-known *pollution effect* [2]. MMP, on the other hand, uses oscillating basis functions (see Section 2.1) which may achieve better approximation properties than the classical piecewise-polynomial spaces of FEM [15].

2 Multiple Multipole Program

The concept of the Multiple Multipole Program was proposed by Ch. Hafner in his dissertation [13] based on the much older work of G. Mie and I.N. Vekua [18,27]. Essentially, the Mie-Vekua approach expands some field in a 2D multiply-connected domain by a multipole expansion supplemented with generalized harmonic polynomials. Extending these ideas, MMP introduces more multipoles (*multiple multipoles*) than required according to Vekua's theory [27].

2.1 Multipoles

Basis functions spanning the MMP Trefftz spaces (2) are the so-called *multipoles*, potentials spawned by (anisotropic) point sources. Multipoles are exact solutions of the homogeneous PDE (1a) that can be subject to the decay condition (1b), depending on whether they are used to approximate the solution in Ω_0 .

A multipole can be written as $v(\mathbf{x}) := f(r_{xc}) g(\theta_{xc})$ in a polar coordinate system in \mathbb{R}^2 ($r \in [0, \infty)$, $\theta \in [0, 2\pi)$) with respect to its center \mathbf{c} ($\mathbf{x}, \mathbf{c} \in \mathbb{R}^2$ are position vectors in Cartesian coordinates). Here, $(r_{xc}, \theta_{xc})^\top$ are polar coordinates of the vector $\mathbf{x}_c := \mathbf{x} - \mathbf{c}$.

The radial dependence $f(r_{xc})$ has a center that may present a singularity, $|f(r)| \rightarrow \infty$ for $r \rightarrow 0$, and the desired decay condition at infinity. If there is a singularity, multipoles have to be centered outside the domain in which they are used for approximation. On the other hand, the angular dependence g is usually formulated in terms of trigonometric functions.

More specifically, the multipoles chosen for the numerical experiments of this work have the forms

$$\begin{aligned} B_0(kr_{xc}), B_1(kr_{xc}) \cos(\theta_{xc}), B_1(kr_{xc}) \sin(\theta_{xc}), \dots, \\ B_\ell(kr_{xc}) \cos(\ell \theta_{xc}), B_\ell(kr_{xc}) \sin(\ell \theta_{xc}), \dots \end{aligned} \quad (3)$$

B_ℓ is a Hankel function of the first kind $H_\ell^{(1)}$ [17, p. 280] or a Bessel function of the first kind J_ℓ [17, p. 278, (9.7)], depending on whether the Trefftz space is for Ω_0 (2a) or Ω_1 (2b). Indeed, multipoles with $H_\ell^{(1)}$ satisfy the decay condition (1b). $k := \omega\sqrt{\epsilon\mu} \in \mathbb{C}$ is the wavenumber k_i in Ω_i , $i = 0, 1$.

Each multipole from (3) is characterized by a location, i.e. its center \mathbf{c} , and the parameter ℓ (its degree). When we place several multipoles at a given location up to a certain order, which is the maximum degree of multipoles with that center, we use the term *multipole expansion*. Summing the number of terms of all multipole expansions used for approximation yields the total number of degrees of freedom of the discretized Trefftz space.

2.2 Approximation Error

Let the solution u of the Helmholtz problem (1a) allow an analytic extension beyond Ω_0 . Then, given a discrete subspace $\mathcal{T}^n(\Omega_0)$ of $\mathcal{T}(\Omega_0)$, u can be approximated by functions in $\mathcal{T}(\Omega_0)$ with an accuracy exponential in $\dim \mathcal{T}^n(\Omega_0)$ with respect to the H^1 -seminorm. This paragraph still holds true if one replaces Ω_0 with Ω_1 .

Both of these convergence results can be proven in the same way as [7, p. 4] for the 2D Poisson's equation, i.e. by relying on the fact that (generalized) harmonic polynomials for approximation also achieve exponential convergence in H^i -seminorms, $i = 0, \dots, j$, $j \in \mathbb{N}_0$, when solving 2D Helmholtz in a bounded domain that satisfies certain assumptions [19, p. 61, Theorem 3.2.5].

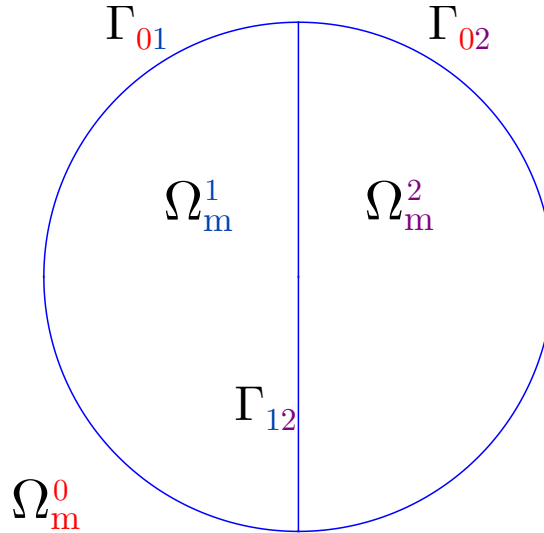


Fig. 1: The geometry represents Ω_m^0 , Ω_m^1 , and Ω_m^2 , the three MMP subdomains with different wavenumbers, and their shared boundaries Γ_{01} , Γ_{02} , and Γ_{12} .

To empirically show the typical convergence of a pure Trefftz discretization, we consider, as in (1), the Helmholtz equation $\nabla^2 u + k^2 u = 0$ subject to the Sommerfeld radiation condition (1b). The domain is \mathbb{R}^2 with a unit disk split into two halves: we call these subdomains Ω_m^0 , Ω_m^1 , and Ω_m^2 (see Figure 1). In each of them, the wavenumber k is referred to as k_1 in one half of the disk (Ω_m^1), k_2 in the other half (Ω_m^2), and k_0 in the complement (Ω_m^0). In Ω_m^0 we also assume that the solution u is decomposable as $u_{\text{incid}} + u_{\text{scatt}}$,

with $u_{\text{incid}} := \exp(ik_0\|\mathbf{x}\|)$ a known plane wave that gives rise to the right-hand side of the problem and u_{scatt} to be determined (compare with (27)).

At the endpoints of the segment splitting the disk in two the solution has triple-point singularities if k_0, k_1, k_2 are all different. Hence, assuming piecewise-constant k , we need to use different Trefftz spaces for each subdomain. Multipoles are then chosen according to (3): Hankel functions are used on the unbounded domain Ω_m^0 , Bessel functions on the bounded domains Ω_m^1, Ω_m^2 .

We consider two configurations of multipoles:

1. Multipole expansions up to a fixed order 1 uniformly located on a circle at the center of each subdomain: $(-0.5, 0)$ for Ω_m^1 , $(0.5, 0)$ for Ω_m^2 , and the origin for Ω_m^0 . Radii are 1.5, 1.5, and 0.5 for Ω_m^1, Ω_m^2 , and Ω_m^0 , respectively. During the convergence test we increase the number of expansions.
2. For each subdomain, one multipole expansion of a given order placed in the origin. During the test we increase this order.

We solve this problem by collocation, imposing *transmission conditions* between multipoles approximating subdomains with different k . Specifically, these conditions are

$$u_m^i|_{\Gamma_{ij}} = u_m^j|_{\Gamma_{ij}}, \quad (4a)$$

$$\mathbf{n} \cdot \nabla u_m^i|_{\Gamma_{ij}} = \mathbf{n} \cdot \nabla u_m^j|_{\Gamma_{ij}}, \quad (4b)$$

with u_m^i MMP solution in Ω_m^i , $i = 0, 1, 2$, $i < j$; in Ω_m^0 , u_m^0 is shifted by the plane wave $\exp(ik_0\|\mathbf{x}\|)$. Γ_{ij} refers to the boundary $\Omega_m^i \cap \Omega_m^j$ (Figure 1), with \mathbf{n} the normal vector. More details on transmission conditions like (4) are given in the next section – see (9).

Matching points for collocation on Γ_{ij} are found through the intersections of conforming meshes on the disk $\Omega_m^1 \cup \Omega_m^2$: these meshes are more refined depending on the number of degrees of freedom of $\mathcal{T}^n(\Omega_m^i)$, $i = 0, 1, 2$, such that the number of matching points is always larger than the sum of the dimensions of the discrete Trefftz spaces (leading to overdetermined systems solved in a least-squares sense by QR decomposition). We use volume meshes to identify matching points on boundaries Γ_{ij} because we want to track a volume error; specifically, the relative approximation error in $H^1(\Omega_m^i)$ -seminorm

$$\int_{\Omega_m^i} \left\| \nabla (u - u_m^i) \right\|_{\ell^2}^2 d\mathbf{x} \quad (5)$$

on bounded domains Ω_m^1, Ω_m^2 . (5) is approximated by a Gaussian quadrature rule that is exact for polynomials of degree 2 (order 3). As benchmark u we rely on the numerical solution that MMP provides with a number of degrees of freedom substantially higher than the highest number used in the convergence study.

Firstly, we consider the case $k_1 = k_2 = 1.59 k_0$ and $k_0 = 7.86 \text{ rad m}^{-1}$, i.e. without TPS. Figure 2 shows the corresponding relative H^1 -errors: we can identify exponential convergence, as expected by [7, p. 4], because in this example the solution possesses analytic extensions beyond the interface.

Conversely, Figure 3 shows these errors for $k_1 = 4 k_0$, $k_2 = 2 k_0$, and $k_0 = 7.86 \text{ rad m}^{-1}$: here we can identify only algebraic convergence. In fact, exponential convergence is not preserved because the solution has a TPS [7, p. 4]. Figure 4 presents more pronounced TPS with $k_1 = 100 k_0$, $k_2 = 10 k_0$, and $k_0 = 7.86 \text{ rad m}^{-1}$: even algebraic convergence becomes difficult to recognize.

We observe that MMP without modifications cannot properly handle TPS or other singularities. There are two ways to cope with this situation:

1. Augmenting the Trefftz spaces with basis functions that capture the singularities [3]. However, explicit knowledge of the form of such singularities is required.
2. Coupling MMP with FEM applied to a locally-refined mesh that encompass the TPS and immediate surrounding regions. This is the approach followed by this work (Section 4.2).

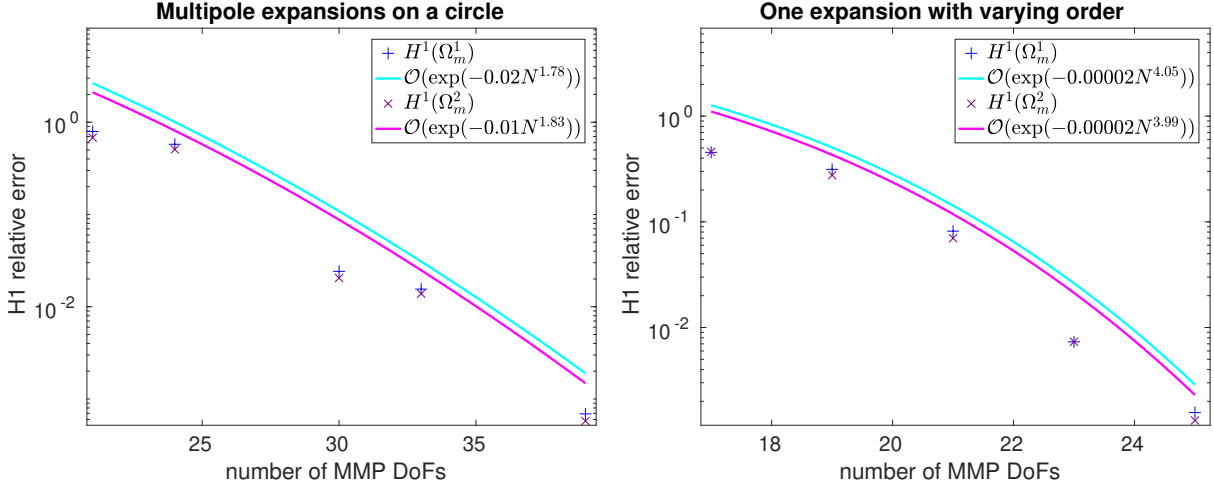


Fig. 2: p -refinement semi-log error plots for 2D Helmholtz equation without TPS solved with three MMP domains (geometry in Figure 1): exponential convergence in $H^1(\Omega_i)$ -seminorm, $i = 1, 2$. Parameters are $k_1 = k_2 = 1.59 k_0$ and $k_0 = 7.86 \text{ rad m}^{-1}$.

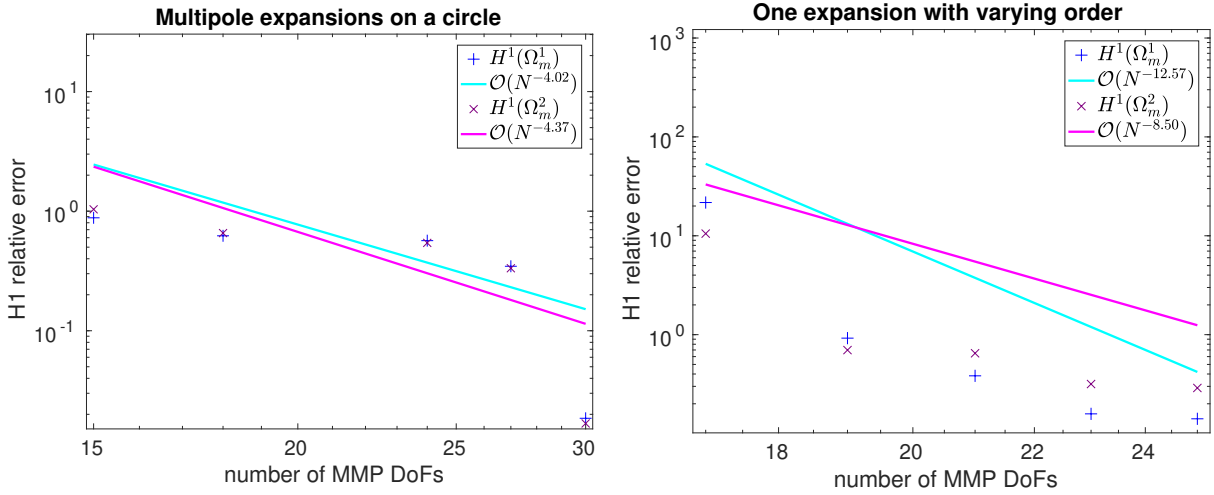


Fig. 3: p -refinement log-log error plots for 2D Helmholtz equation with TPS solved with three MMP domains (geometry in Figure 1): algebraic convergence in $H^1(\Omega_i)$ -seminorm, $i = 1, 2$. Parameters are $k_1 = 4 k_0$, $k_2 = 2 k_0$, and $k_0 = 7.86 \text{ rad m}^{-1}$.

3 Coupling Strategies

We consider the partition (refer to Figure 5b)

$$\mathbb{R}^2 = \Omega_f \cup \Omega_m^0 \cup \Omega_m^1 \cup \Gamma_{f0} \cup \Gamma_{f1} \cup \Gamma_{01}, \quad (6)$$

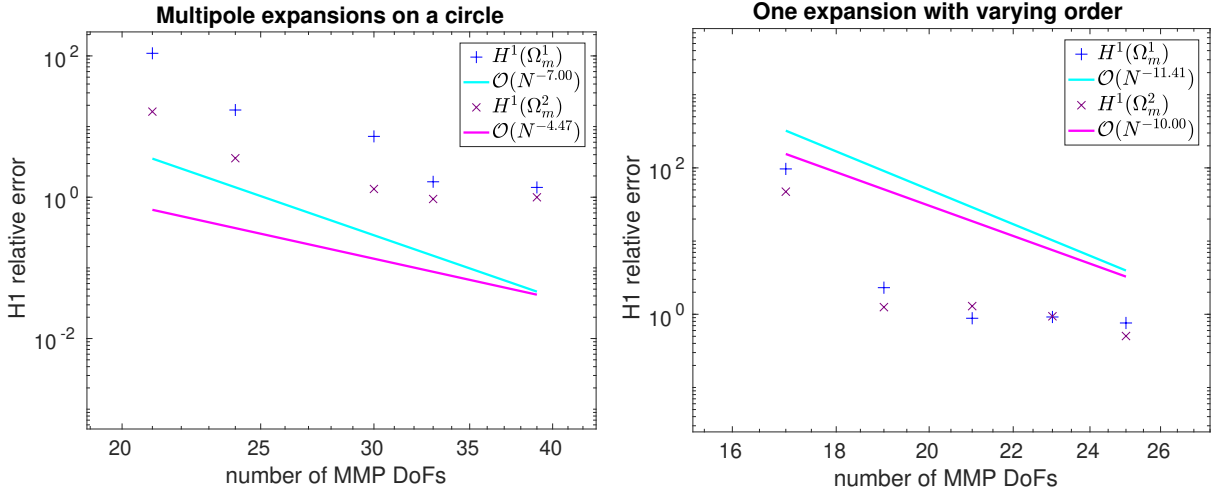


Fig. 4: p -refinement log-log error plots for 2D Helmholtz equation with TPS solved with three MMP domains (geometry in Figure 1): algebraic convergence in $H^1(\Omega_i)$ -seminorm, $i = 1, 2$. Parameters are $k_1 = 100 k_0$, $k_2 = 10 k_0$, and $k_0 = 7.86 \text{ rad m}^{-1}$.

with $\Gamma_{f0} := \partial\Omega_f \cap \partial\Omega_m^0$, $\Gamma_{f1} := \partial\Omega_f \cap \partial\Omega_m^1$, $\Gamma_{01} := \partial\Omega_m^0 \cap \partial\Omega_m^1$ and $\Omega_f \cap \Omega_m^0 = \emptyset$, $\Omega_f \cap \Omega_m^1 = \emptyset$, $\Omega_m^0 \cap \Omega_m^1 = \emptyset$. We also define $\Omega_m := \Omega_m^0 \cup \Omega_m^1$ and the skeleton $\Gamma := \Gamma_{f0} \cup \Gamma_{f1} \cup \Gamma_{01}$.

We call Ω_f , a bounded Lipschitz domain, the FEM domain, whereas Ω_m^0 is the unbounded and Ω_m^1 the bounded MMP domain. The terminology indicates the type of approximation to be employed in each domain. Coupling between the FEM and MMP domains is done across the interfaces Γ_{fi} , $i = 0, 1$, while coupling between the two MMP domains occurs across the interface Γ_{01} .

We demand $\Omega_\star \subset \Omega_f$, but not necessarily $\Omega_\star = \Omega_f$. If $\Omega_\star \neq \Omega_f$, $\Gamma_{f0} \cup \Gamma_{f1} = \partial\Omega_f$ is an *artificial interface*. Note that Ω_f can be composed of disjoint regions (Figure 15).

We also demand that in Ω_m^0, Ω_m^1 the equation parameters of (1a) are constant: $\Omega_m^i \subset \Omega_i$, $i = 0, 1$, given the partition introduced in Section 1, i.e. constant wavenumbers k_0, k_1 for Ω_m^0, Ω_m^1 . Hence, the Trefftz spaces $\mathcal{T}(\Omega_m^0), \mathcal{T}(\Omega_m^1)$ are still defined according to (2).

We now define the *magnetic (“Neumann”) trace operator* γ :

$$\gamma : H^1(\nabla^2, \Omega_\square) \rightarrow \tilde{H}^{-\frac{1}{2}}(\Gamma_\square), \quad \gamma v := \mathbf{n} \cdot \mathbf{M}_\epsilon^{-1} \nabla v, \quad v \in H^1(\nabla^2, \Omega_\square). \quad (7)$$

- $\Omega_\square \in \{\Omega_f, \Omega_m^0, \Omega_m^1\}$ and $\Gamma_\square \in \{\Gamma_{f0}, \Gamma_{f1}, \Gamma_{01}\}$.
- $H^1(\nabla^2, \Omega_\square)$ is the space of functions $v \in H^1(\Omega_\square)$ for which $\nabla^2 v \in L^2(\Omega_\square)$.
- $\tilde{H}^{-\frac{1}{2}}(\Gamma_\square)$ is the dual space of $H^{\frac{1}{2}}(\Gamma_\square)$ [22, p. 59, (2.90)], to which the Dirichlet traces $v|_{\Gamma_\square}$ belong.
- \mathbf{n} is the normal vector on Γ_\square .

We also define

$$u_f := u|_{\Omega_f} \in H^1(\Omega_f), \quad u_m^0 := u|_{\Omega_m^0} \in H_{\text{loc}}^1(\Omega_m^0), \quad u_m^1 := u|_{\Omega_m^1} \in H^1(\Omega_m^1). \quad (8)$$

Using this notation, we can write the transmission conditions that the solution of (1) has to satisfy across Γ_{fi} , $i = 0, 1$ [20, p. 107, Lemma 5.3]:

$$u_f|_{\Gamma_{fi}} = u_m^i|_{\Gamma_{fi}}, \quad (9a)$$

$$\gamma u_f|_{\Gamma_{fi}} = \gamma u_m^i|_{\Gamma_{fi}}. \quad (9b)$$

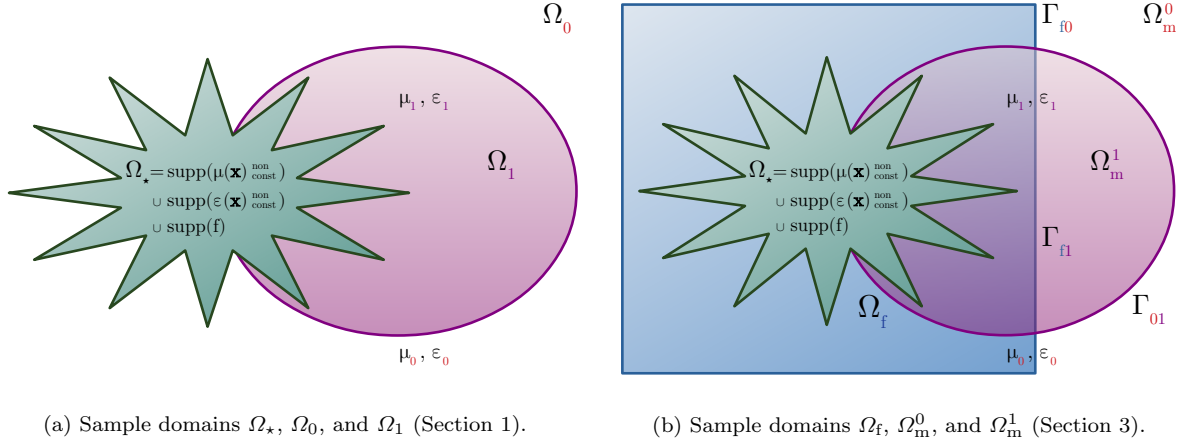


Fig. 5: Physical domains (Figure 5a) do not necessarily correspond to computational domains (Figure 5b): Γ_{f0} , Γ_{f1} can be artificial interfaces. Different colors in the figure represent regions with different parameters ϵ , μ .

The same conditions hold across Γ_{01} .

Transmission conditions (9) on Γ_{f0} , Γ_{f1} , Γ_{01} and the weak form of (1a) in Ω_f are all the ingredients to obtain a FEM–MMP coupled solution of (1). By testing the weak form of (1a) with suitable test functions, integrating by parts over Ω_f , and using the transmission condition (9b) on Γ_{f0} , Γ_{f1} , we obtain

$$\int_{\Omega_f} [(\mathbf{M}_\epsilon^{-1} \nabla u_f) \cdot \nabla v_f - \omega^2 \mu u_f v_f] \, d\mathbf{x} - \int_{\Gamma_{f0}} \gamma u_m^0 v_f \, dS - \int_{\Gamma_{f1}} \gamma u_m^1 v_f \, dS = \int_{\Omega_f} f v_f \, d\mathbf{x} \quad (10)$$

$$\forall v_f \in H^1(\Omega_f).$$

We end up with different coupling approaches depending on how we impose the additional transmission condition (9a) on Γ_{f0} , Γ_{f1} and both transmission conditions (9) on Γ_{01} . These coupling approaches are discussed in the following sections as stationary points for different *Lagrangian functionals*. The resulting *linear variational saddle-point problems* are also stated.

Discretization Throughout we use triangular meshes \mathcal{M}_f on Ω_f and simple polygonal approximations of Γ_{01} for the sake of numerical integration.

We discretize $u_f \in H^1(\Omega_f)$ with piecewise-linear Lagrangian finite elements, i.e.

$$V^n(\mathcal{M}_f) = \mathcal{S}_1^0(\mathcal{M}_f) := \left\{ v^n \in C^0(\Omega_f) : v^n|_K(\mathbf{x}) = a_K + \mathbf{b}_K \cdot \mathbf{x}, \right. \\ \left. a_K \in \mathbb{R}, \mathbf{b}_K \in \mathbb{R}^2, \mathbf{x} \in K \quad \forall K \in \mathcal{M}_f \right\}. \quad (11)$$

For Ω_m^0 , Ω_m^1 we let a finite number of multipoles span the discrete Trefftz spaces $\mathcal{T}^n(\Omega_m^i) \subset \mathcal{T}(\Omega_m^i)$, $i = 0, 1$. The dimension of each $\mathcal{T}^n(\Omega_m^i)$ is determined by the number of multipole expansions chosen for the approximation and their orders.

3.1 PDE-constrained Least-Squares Coupling

Taking the cue from (9a), we seek $u_f \in H^1(\Omega_f)$, $u_m^0 \in \mathcal{T}(\Omega_m^0)$, and $u_m^1 \in \mathcal{T}(\Omega_m^1)$

1. minimizing

$$\begin{aligned} J_\Gamma(u_f, u_m^0, u_m^1) := & \|u_f - u_m^0\|_{H^{\frac{1}{2}}(\Gamma_{f0})}^2 + \|u_f - u_m^1\|_{H^{\frac{1}{2}}(\Gamma_{f1})}^2 + \\ & \|u_m^0 - u_m^1\|_{H^{\frac{1}{2}}(\Gamma_{01})}^2 + \|\gamma(u_m^0 - u_m^1)\|_{H^{-\frac{1}{2}}(\Gamma_{01})}^2 \end{aligned} \quad (12)$$

2. and satisfying the constraint (10).

These two conditions determine a quadratic minimization problem under a linear variational constraint where we switch the usual meaning of these two components: here the constraint is given by the variational form of the minimization problem that satisfies the system of PDEs (1a) in Ω_f , while the functional J_Γ to be minimized is composed of the transmission conditions not imposed by the FEM variational form.

This problem can be rephrased as seeking a saddle point of the following Lagrangian:

$$\begin{aligned} L(u_f, u_m^0, u_m^1, p_f) := & \frac{1}{2} J_\Gamma(u_f, u_m^0, u_m^1) + \\ & \int_{\Omega_f} \left[(\mathbf{M}_\epsilon^{-1} \nabla u_f) \cdot \nabla p_f - \omega^2 \mu u_f p_f \right] d\mathbf{x} - \int_{\Gamma_{f0}} \gamma u_m^0 p_f dS - \int_{\Gamma_{f1}} \gamma u_m^1 p_f dS - \int_{\Omega_f} f p_f d\mathbf{x}, \end{aligned} \quad (13)$$

where $p_f \in H^1(\Omega_f)$ is the Lagrange multiplier imposing (10).

The norms $\|\cdot\|_{H^{\pm\frac{1}{2}}(\Gamma_\square)}$ for any $\Gamma_{f0}, \Gamma_{f1}, \Gamma_{01}$ are nonlocal. Thus, for practicality we replace them with the $L^2(\Gamma_\square)$ -norm in (12). Given this substitution, the necessary and sufficient optimality conditions of (13) give rise to the saddle-point problem

$$\begin{aligned} & \text{Seek } u_f \in H^1(\Omega_f), u_m^0 \in \mathcal{T}(\Omega_m^0), u_m^1 \in \mathcal{T}(\Omega_m^1), p_f \in H^1(\Omega_f): \\ & \begin{cases} \text{a}_{\text{LS}}[(u_f, u_m^0, u_m^1), (v_f, v_m^0, v_m^1)] + \text{b}_{\text{LS}}[(v_f, v_m^0, v_m^1), p_f] = 0 \\ \text{b}_{\text{LS}}[(u_f, u_m^0, u_m^1), q_f] = \int_{\Omega_f} f q_f d\mathbf{x} \end{cases} \\ & \forall v_f \in H^1(\Omega_f), \forall v_m^0 \in \mathcal{T}(\Omega_m^0), \forall v_m^1 \in \mathcal{T}(\Omega_m^1), \forall q_f \in H^1(\Omega_f), \end{aligned} \quad (14)$$

where

$$\begin{aligned} \text{a}_{\text{LS}} \left[(u_f, u_m^0, u_m^1), (v_f, v_m^0, v_m^1) \right] := & \\ & \int_{\Gamma_{f0}} (u_f - u_m^0) (v_f - v_m^0) dS + \int_{\Gamma_{f1}} (u_f - u_m^1) (v_f - v_m^1) dS + \\ & \int_{\Gamma_{01}} \left[(u_m^0 - u_m^1) (v_m^0 - v_m^1) + \gamma (u_m^0 - u_m^1) \gamma (v_m^0 - v_m^1) \right] dS, \end{aligned} \quad (15a)$$

$$\begin{aligned} \text{b}_{\text{LS}} \left[(u_f, u_m^0, u_m^1), q_f \right] := & \\ & \int_{\Omega_f} \left[(\mathbf{M}_\epsilon^{-1} \nabla u_f) \cdot \nabla q_f - \omega^2 \mu u_f q_f \right] d\mathbf{x} + \int_{\Gamma_{f0}} \gamma u_m^0 q_f dS + \int_{\Gamma_{f1}} \gamma u_m^1 q_f dS. \end{aligned} \quad (15b)$$

Discretization We propose the following discretization for (14):

- $u_f, v_f, p_f, q_f \in V^n(\mathcal{M}_f)$ of (11),
- $u_m^0, v_m^0 \in \mathcal{T}^n(\Omega_m^0)$, and
- $u_m^1, v_m^1 \in \mathcal{T}^n(\Omega_m^1)$.

3.2 Multi-Field Coupling

The *multi-field domain decomposition method* allows to use FEM with nonconforming meshes on different neighboring domains for the same boundary value problem [5]. This is well-suited for the coupling because one can think of MMP as FEM with special trial and test functions used on a “mesh” with two entities: Ω_m^0 and Ω_m^1 .

The multi-field approach imposes the continuity (9a) for any $\Gamma_{f0}, \Gamma_{f1}, \Gamma_{01}$ in a weak sense by means of Lagrange multipliers: $\lambda_{f0}, \lambda_{f1}, \lambda_{01}$. Note that (9a) is an equation connecting traces in $H^{\frac{1}{2}}(\Gamma_\square)$, and therefore any λ_\square has to belong to the dual space $\tilde{H}^{-\frac{1}{2}}(\Gamma_\square)$.

Hence, the multi-field coupling can be expressed by the following Lagrangian:

$$\begin{aligned} L(u_f, u_m^0, u_m^1, \lambda_{f0}, \lambda_{f1}, \lambda_{01}) &:= J_{\Omega_f}(u_f) + J_{\Omega_m}(u_m^0, u_m^1) + \\ &\int_{\Gamma_{f0}} (u_f - u_m^0) \lambda_{f0} \, dS + \int_{\Gamma_{f1}} (u_f - u_m^1) \lambda_{f1} \, dS + \int_{\Gamma_{01}} (u_m^0 - u_m^1) \lambda_{01} \, dS, \end{aligned} \quad (16)$$

where $\lambda_{f0}, \lambda_{f1}, \lambda_{01}$ belong to $\tilde{H}^{-\frac{1}{2}}(\Gamma_{f0}), \tilde{H}^{-\frac{1}{2}}(\Gamma_{f1}), \tilde{H}^{-\frac{1}{2}}(\Gamma_{01})$, respectively.

The functional J_{Ω_f} expresses the saddle-point problem that satisfies (1a) in Ω_f :

$$J_{\Omega_f}(u_f) := \frac{1}{2} \int_{\Omega_f} \left[(\mathbf{M}_\epsilon^{-1} \nabla u_f) \cdot \nabla u_f - \omega^2 \mu |u_f|^2 \right] \, d\mathbf{x} - \int_{\Omega_f} f u_f \, d\mathbf{x}. \quad (17a)$$

The functional J_{Ω_m} for u_m^0, u_m^1 has a similar formulation, but for homogeneous problems:

$$J_{\Omega_m}(u_m^0, u_m^1) := \frac{1}{2} \int_{\Omega_m^0} \left(\|\nabla u_m^0\|_{\ell^2}^2 - k_0^2 |u_m^0|^2 \right) \, d\mathbf{x} + \frac{1}{2} \int_{\Omega_m^1} \left(\|\nabla u_m^1\|_{\ell^2}^2 - k_1^2 |u_m^1|^2 \right) \, d\mathbf{x}. \quad (17b)$$

Because $u_m^i \in \mathcal{T}(\Omega_m^i)$, $i = 0, 1$, one can rewrite the volume integrals in (17b) as boundary integrals:

$$\frac{1}{2} \int_{\Omega_m^i} \left(\|\nabla u_m^i\|_{\ell^2}^2 - k_i^2 |u_m^i|^2 \right) \, d\mathbf{x} = \frac{1}{2} \int_{\partial\Omega_m^i} \gamma u_m^i u_m^i \, dS. \quad (17c)$$

The signs of the boundary integrals in (17c) are set by choosing \mathbf{n} pointing outwards from Ω_m^i , $i = 0, 1$.

We finally obtain the following saddle-point problem:

$$\begin{aligned} &\text{Seek } u_f \in H^1(\Omega_f), u_m^0 \in \mathcal{T}(\Omega_m^0), u_m^1 \in \mathcal{T}(\Omega_m^1), \\ &\lambda_{f0} \in \tilde{H}^{-\frac{1}{2}}(\Gamma_{f0}), \lambda_{f1} \in \tilde{H}^{-\frac{1}{2}}(\Gamma_{f1}), \lambda_{01} \in \tilde{H}^{-\frac{1}{2}}(\Gamma_{01}): \\ &\begin{cases} \mathbf{a}_{\text{MF}}[(u_f, u_m^0, u_m^1), (v_f, v_m^0, v_m^1)] + \mathbf{b}_{\text{MF}}[(v_f, v_m^0, v_m^1), (\lambda_{f0}, \lambda_{f1}, \lambda_{01})] = \int_{\Omega_f} f v_f \, d\mathbf{x} \\ \mathbf{b}_{\text{MF}}[(u_f, u_m^0, u_m^1), (\chi_{f0}, \chi_{f1}, \chi_{01})] = 0 \end{cases} \quad (18) \\ &\forall v_f \in H^1(\Omega_f), \forall v_m^0 \in \mathcal{T}(\Omega_m^0), \forall v_m^1 \in \mathcal{T}(\Omega_m^1), \\ &\forall \chi_{f0} \in \tilde{H}^{-\frac{1}{2}}(\Gamma_{f0}), \forall \chi_{f1} \in \tilde{H}^{-\frac{1}{2}}(\Gamma_{f1}), \forall \chi_{01} \in \tilde{H}^{-\frac{1}{2}}(\Gamma_{01}), \end{aligned}$$

where

$$\begin{aligned} a_{\text{MF}} \left[\left(u_f, u_m^0, u_m^1 \right), \left(v_f, v_m^0, v_m^1 \right) \right] &:= \int_{\Omega_f} \left[\left(\mathbf{M}_\epsilon^{-1} \nabla u_f \right) \cdot \nabla v_f - \omega^2 \mu u_f v_f \right] dx \\ &\quad + \int_{\partial\Omega_m^0} \gamma u_m^0 v_m^0 dS + \int_{\partial\Omega_m^1} \gamma u_m^1 v_m^1 dS, \end{aligned} \quad (19a)$$

$$\begin{aligned} b_{\text{MF}} \left[\left(u_f, u_m^0, u_m^1 \right), \left(\chi_{f0}, \chi_{f1}, \chi_{01} \right) \right] &:= \int_{\Gamma_{f0}} \left(u_f - u_m^0 \right) \chi_{f0} dS + \int_{\Gamma_{f1}} \left(u_f - u_m^1 \right) \chi_{f1} dS \\ &\quad + \int_{\Gamma_{01}} \left(u_m^0 - u_m^1 \right) \chi_{01} dS. \end{aligned} \quad (19b)$$

Discretization For the discretization of (18), we suggest $u_f, v_f \in V^n(\mathcal{M}_f)$ of (11), $u_m^0, v_m^0 \in \mathcal{T}^n(\Omega_m^0)$, and $u_m^1, v_m^1 \in \mathcal{T}^n(\Omega_m^1)$.

The discretization of $\lambda_{f0}, \lambda_{f1}, \lambda_{01} \in \tilde{H}^{-\frac{1}{2}}(\Gamma_\square)$ is a topic debated in the literature [21, Section 4]. In the spirit of *mortar element methods*, we opt for the Dirichlet traces on each Γ_\square of the trial space used to discretize one of the neighboring domains [21, p. B426]:

- for λ_{fi} , $i = 0, 1$, the Dirichlet traces on each Γ_{fi} of the elements in the piecewise-linear space $V^n(\mathcal{M}_f) \subset H^1(\Omega_f)$;
- for λ_{01} , the Dirichlet traces on Γ_{01} of the multipoles in either $\mathcal{T}^n(\Omega_m^0)$ or $\mathcal{T}^n(\Omega_m^1)$.

3.3 Discontinuous Galerkin

As for the multi-field coupling (Section 3.2), we again treat each MMP discretization as a finite element method with special functions. Here we exploit the other main approach for imposing weak continuity on nonconforming meshes, which is the *Discontinuous Galerkin* (DG) method [1].

Following this idea, the coupling can be expressed as a *discrete* minimization problem for the following Lagrangian:

$$\begin{aligned} L(u_f^n, u_m^{n,0}, u_m^{n,1}) &:= J_{\Omega_f}(u_f^n) + J_{\Omega_m}(u_m^{n,0}, u_m^{n,1}) + \int_{\Gamma_{f0}} \left(u_f^n - u_m^{n,0} \right) P^n(u_f^n, u_m^{n,0}) dS \\ &\quad + \int_{\Gamma_{f1}} \left(u_f^n - u_m^{n,1} \right) P^n(u_f^n, u_m^{n,1}) dS + \int_{\Gamma_{01}} \left(u_m^{n,0} - u_m^{n,1} \right) P^n(u_m^{n,0}, u_m^{n,1}) dS, \end{aligned} \quad (20)$$

where J_{Ω_f} and J_{Ω_m} are the same as in (17a) and (17b). $u_f^n \in V^n(\mathcal{M}_f)$ of (11), $u_m^{n,0} \in \mathcal{T}^n(\Omega_m^0)$, and $u_m^{n,1} \in \mathcal{T}^n(\Omega_m^1)$.

Depending on the choice of the operator $P^n : H^{\frac{1}{2}}(\Gamma_\square) \times H^{\frac{1}{2}}(\Gamma_\square) \rightarrow \tilde{H}^{-\frac{1}{2}}(\Gamma_\square)$, we obtain different DG approaches. We follow the (symmetric) *Interior Penalty DG method* [25]:

$$P^n(u, v) := -\mathbf{n} \cdot \overline{\mathbf{M}}_\epsilon^{-1} \nabla(u + v) + \eta \bar{\epsilon}^{-1}(u - v). \quad (21)$$

- $\overline{\mathbf{M}}_\epsilon(\mathbf{x}) : \mathbb{R}^2 \rightarrow \mathbb{C}^{2,2}$ is the mean of material parameters \mathbf{M}_ϵ in Ω_f and Ω_m^i when integrating on each Γ_{fi} , $i = 0, 1$:

$$\overline{\mathbf{M}}_\epsilon(\mathbf{x}) := \frac{\mathbf{M}_\epsilon(\mathbf{x}) + \epsilon_i \mathbf{I}}{2} \quad \forall \mathbf{x} \in \Gamma_{fi}, \quad (22)$$

and of \mathbf{M}_ϵ in Ω_m^0 and Ω_m^1 when integrating on Γ_{01} :

$$\overline{\mathbf{M}}_\epsilon(\mathbf{x}) := \frac{\epsilon_0 + \epsilon_1}{2} \mathbf{I} \quad \forall \mathbf{x} \in \Gamma_{01}. \quad (23)$$

- $\eta \in \mathbb{R}$ is a penalty parameter that needs to be assigned heuristically. On any Γ_{fi} , $i = 0, 1$, η should be proportional to N_m^i/h , where N_m^i is the number of degrees of freedom of $\mathcal{T}^n(\Omega_m^i)$ and $h \in \mathbb{R}$ the meshwidth of \mathcal{M}_f restricted to Γ_{fi} . On Γ_{01} , η should be proportional to $N_m^0 N_m^1$. Both choices are inspired by $\eta \sim p^2/h$, setting used in case of polynomial DG-FEM [26, p. 229] (with $p \in \mathbb{N}^*$ polynomial degree).

Finding the stationary point of (20) leads to the discrete problem

$$\begin{aligned} & \text{Seek } u_f^n \in V^n(\mathcal{M}_f), u_m^{n,0} \in \mathcal{T}^n(\Omega_m^0), u_m^{n,1} \in \mathcal{T}^n(\Omega_m^1): \\ & a_{\text{DG}}^n \left[\left(u_f^n, u_m^{n,0}, u_m^{n,1} \right), \left(v_f^n, v_m^{n,0}, v_m^{n,1} \right) \right] = \int_{\Omega_f} f v_f^n \, d\mathbf{x} \\ & \forall v_f^n \in V^n(\mathcal{M}_f), \forall v_m^{n,0} \in \mathcal{T}^n(\Omega_m^0), \forall v_m^{n,1} \in \mathcal{T}^n(\Omega_m^1), \end{aligned} \quad (24)$$

where we define the symmetric bilinear form $a_{\text{DG}}^n(\cdot, \cdot)$ as

$$\begin{aligned} & a_{\text{DG}}^n \left[\left(u_f^n, u_m^{n,0}, u_m^{n,1} \right), \left(v_f^n, v_m^{n,0}, v_m^{n,1} \right) \right] := \int_{\Omega_f} \left[\left(\mathbf{M}_\epsilon^{-1} \nabla u_f^n \right) \cdot \nabla v_f^n - \omega^2 \mu u_f^n v_f^n \right] d\mathbf{x} - \\ & \sum_{i=0,1} \int_{\Gamma_{fi}} \left\{ \left[\gamma \left(u_f^n + u_m^{n,i} \right) \right] \left(v_f^n - v_m^{n,i} \right) + \left(u_f^n - u_m^{n,i} \right) \left[\gamma \left(v_f^n + v_m^{n,i} \right) \right] \right\} dS + \\ & \sum_{i=0,1} \int_{\Gamma_{ii}} 2\eta \left(u_f^n - u_m^{n,i} \right) \left(v_f^n - v_m^{n,i} \right) dS + \sum_{i=0,1} \int_{\partial\Omega_m^i} \gamma u_m^i v_m^i dS - \\ & \int_{\Gamma_{01}} \left\{ \left[\gamma \left(u_m^{n,0} + u_m^{n,1} \right) \right] \left(v_m^{n,0} - v_m^{n,1} \right) + \left(u_m^{n,0} - u_m^{n,1} \right) \left[\gamma \left(v_m^{n,0} + v_m^{n,1} \right) \right] \right\} dS + \\ & \int_{\Gamma_{01}} 2\eta \left(u_m^{n,0} - u_m^{n,1} \right) \left(v_m^{n,0} - v_m^{n,1} \right) dS. \end{aligned} \quad (25)$$

4 Numerical Results

Throughout we use piecewise-linear Lagrangian finite elements, i.e. $V^n(\mathcal{M}_f) = \mathcal{S}_1^0(\mathcal{M}_f)$ of (11), on triangular meshes \mathcal{M}_f of Ω_f . To study the convergence we employ uniform h -refinement of \mathcal{M}_f and p -refinement of the Trefftz approximations, in the sense that we increase the number of multipoles. The p -refinement of the multipoles forming $\mathcal{T}^n(\Omega_m^i)$, $i = 0, 1$, is linked to the h -refinement of \mathcal{M}_f ; specifically, to the logarithm of the number of intersections of the mesh entities of \mathcal{M}_f on Γ_{fi} . This choice is motivated by the exponential convergence of the MMP approximation error (see Section 2.2).

Here we monitor the following errors:

- The volume errors in the bounded domains Ω_f, Ω_m^1 . These are the relative $L^2(\Omega_f)$ - and $L^2(\Omega_m^1)$ -errors of the FEM and MMP (in Ω_m^1) approximations compared to the reference solution u , i.e.

$$\begin{aligned} & \left\| u - \sum_{j=1}^{N_f} \alpha_f^j v_f^j(\mathbf{x}) \right\|_{L^2(\Omega_f)} \Big/ \|u\|_{L^2(\Omega_f)} \quad \text{and} \\ & \left\| u - \sum_{j=1}^{N_m^1} \alpha_m^{j,1} v_m^{j,1}(\mathbf{x}) \right\|_{L^2(\Omega_m^1)}^2 \Big/ \|u\|_{L^2(\Omega_m^1)}, \end{aligned} \quad (26)$$

with $\alpha_f^j, \alpha_m^{j,1} \in \mathbb{C}$, $v_f^j \in V^n(\mathcal{M}_f)$, $v_m^{j,1} \in \mathcal{T}^n(\Omega_m^1)$, and N_f, N_m^1 numbers of degrees of freedom of the discrete spaces $V^n(\mathcal{M}_f)$ and $\mathcal{T}^n(\Omega_m^1)$, respectively.

On the bounded MMP domain Ω_m^1 we define an auxiliary volume mesh for the numerical quadrature of the error (26). However, on top of \mathcal{M}_f , only a mesh on the 1-dimensional hypersurface Γ_{01} is really necessary for the coupling, in order to compute the numerical integrals on that interface.

- The boundary error on $\partial\Omega_m^0 = \Gamma_{f0} \cup \Gamma_{01}$, union of the (bounded) interfaces between the unbounded domain Ω_m^0 and the other (bounded) domains Ω_f, Ω_m^1 . This is the relative $L^2(\partial\Omega_m^0)$ -error of the MMP approximation in Ω_m^0 compared to the reference solution.

The sum of the relative $L^2(\Omega_f)$ - and $L^2(\Omega_m^1)$ -errors and the relative $L^2(\partial\Omega_m^0)$ -error is the total relative error of the coupling.

We can ignore the impact of numerical integration for FEM because we use a local Gaussian quadrature rule that is exact for polynomials of degree 2 (order 3).

Implementation Meshes were generated using `Gmsh` [10]. Our code is written in `C++14`, using `C++11` multithreading for parallelization. We use `Eigen` v3.3.7 [12] for linear algebra and `HyDi` [6] for the FEM component. The `PARDISO` v6.0 solver [23] provides the sparse LU decomposition to solve the systems of the coupling, characterized by nontrivial sparsity patterns.

4.1 2D Scattering Problem with Exact Solution

We solve $\nabla \cdot (\epsilon^{-1} \nabla u) + \omega^2 \mu u = 0$ in \mathbb{R}^2 subject to the Sommerfeld radiation condition (1b) with piecewise-constant permittivity $\epsilon = 100 \epsilon_0$ in a unit disk centered in the origin, which we dub Ω_\bullet , and $\epsilon = \epsilon_0 = 8.85 \cdot 10^{-12} \text{ F m}^{-1}$ (permittivity of free space) elsewhere. μ and ω are everywhere equal to $\mu_0 = 4\pi \cdot 10^{-7} \text{ H s}^{-1}$ (permeability of free space) and $23.56 \cdot 10^7 \text{ rad s}^{-1}$, respectively. Wavenumbers are therefore $k_\bullet = 10 k_0$ in Ω_\bullet and $k_0 = 0.79 \text{ rad m}^{-1}$ elsewhere.

We assume that u is subject to an excitation by an incident plane wave propagating along the x -axis outside Ω_\bullet , i.e.

$$u = u_{\text{incid}} + u_{\text{scatt}} \text{ in } \mathbb{R}^2 \setminus \Omega_\bullet, \quad u_{\text{incid}} := \exp(ik_0 \|\mathbf{x}\|), \quad \mathbf{x} := (x_1, x_2)^\top, \quad (27)$$

where u_{scatt} represents the unknown scattered potential. This problem has an exact solution that can be derived using *Mie theory* [4, Chapter 4, pp. 82–101] in 2D:

$$\begin{aligned} u &= u_{\text{incid}} + u_{\text{scatt}} = \sum_{\ell=-\infty}^{\infty} i^\ell J_\ell(k_0 r) e^{i\ell\theta} + \sum_{\ell=-\infty}^{\infty} A_\ell H_\ell^{(1)}(k_0 r) e^{i\ell\theta} \text{ in } \mathbb{R}^2 \setminus \Omega_\bullet, \\ u &= u_{\text{refr}} = \sum_{\ell=-\infty}^{\infty} B_\ell J_\ell(k_\bullet r) e^{i\ell\theta} \text{ in } \Omega_\bullet. \end{aligned} \quad (28)$$

Here u_{incid} is the Jacobi–Anger expansion of the exciting plane wave [9, p. 33, (2.46)], given J_ℓ and $H_\ell^{(1)}$ Bessel and Hankel functions of the first kind and $r \in [0, \infty)$, $\theta \in [0, 2\pi)$ canonical polar coordinate system in \mathbb{R}^2 (see Section 2.1). u_{refr} is the unknown refracted potential.

Coefficients A_ℓ, B_ℓ in (28) are

$$\begin{aligned} A_\ell &= i^\ell \frac{\epsilon_\bullet^{-1} k_\bullet J_\ell(k_0 r_\bullet) J'_\ell(k_\bullet r_\bullet) - \epsilon_0^{-1} k_0 J_\ell(k_\bullet r_\bullet) J'_\ell(k_0 r_\bullet)}{\epsilon_0^{-1} k_0 H_\ell^{(1)}(k_0 r_\bullet) J_\ell(k_\bullet r_\bullet) - \epsilon_\bullet^{-1} k_\bullet H_\ell^{(1)}(k_0 r_\bullet) J'_\ell(k_\bullet r_\bullet)}, \\ B_\ell &= \frac{A_\ell H_\ell^{(1)}(k_0 r_\bullet) + i^\ell J_\ell(k_0 r_\bullet)}{J_\ell(k_\bullet r_\bullet)}. \end{aligned} \quad (29)$$

r_\bullet is the radius of the disk Ω_\bullet , here = 1 m.

For our numerical tests, we consider the terms in the expansions of (28) for $\ell = 0, \dots, 20$, identify Ω_\bullet with Ω_f and $\mathbb{R}^2 \setminus \Omega_\bullet$ with a single MMP domain Ω_m , and therefore set $\Gamma := \partial\Omega_f \cap \partial\Omega_m$ on the physical boundary of the disk. Given that we use triangular meshes, Γ is actually a polygonal approximation of a circle.

$\mathcal{T}^n(\Omega_m)$ is generated by a single multipole expansion centered in the origin.

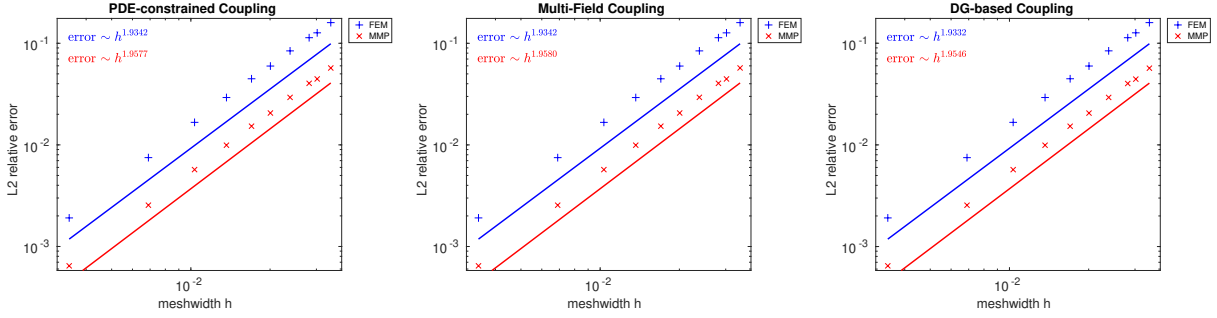


Fig. 6: h -refinement log-log error plots for 2D Helmholtz equation with exact solution. Parameters are $\epsilon_\bullet = 100 \epsilon_0$ and $\omega = 23.56 \cdot 10^7 \text{ rad s}^{-1}$.

Figure 6 shows h -refinement convergence plots for all coupling approaches, which yield very similar results. We can clearly see algebraic convergence of the FEM and MMP errors with rate 2.

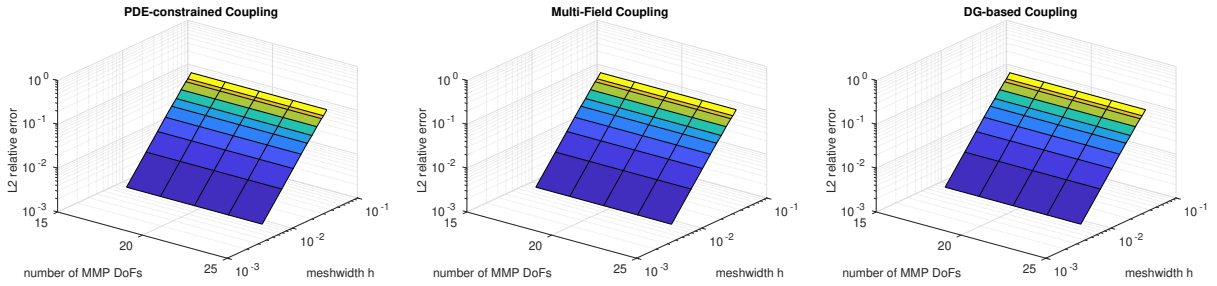


Fig. 7: Meshwidth h vs. MMP degrees of freedom for 2D Helmholtz equation with exact solution: total relative error. The h - and error-dimensions are in logarithmic scale. Parameters are $\epsilon_\bullet = 100 \epsilon_0$ and $\omega = 23.56 \cdot 10^7 \text{ rad s}^{-1}$.

Figure 7 shows surface plots of the total relative L^2 -error for all coupling approaches. The error decreases with h (algebraic convergence) and is generally independent from the number of multipoles: the FEM error dominates. This is a consequence of the exponential convergence of MMP (Section 2.2): the exact solution is so easy to approximate in the MMP domain that it can already be represented by a multipole expansion of the lowest considered order, which is 8, leading to 17 terms of the expansion – see (3).

We have also considered different material parameters, leading to similar convergence rates. For example, Figure 8 shows h -refinement convergence plots for $\epsilon_\bullet = 2.5281 \epsilon_0$ and $\omega = 23.56 \cdot 10^8 \text{ rad s}^{-1}$, which entails $k_\bullet = 1.59 k_0$ and $k_0 = 7.86 \text{ rad m}^{-1}$. Datapoints are slightly noisier than before because we consider a higher

value for the frequency ω , which causes the pollution effect for FEM. However, with these parameters one can observe an interesting physical phenomenon.

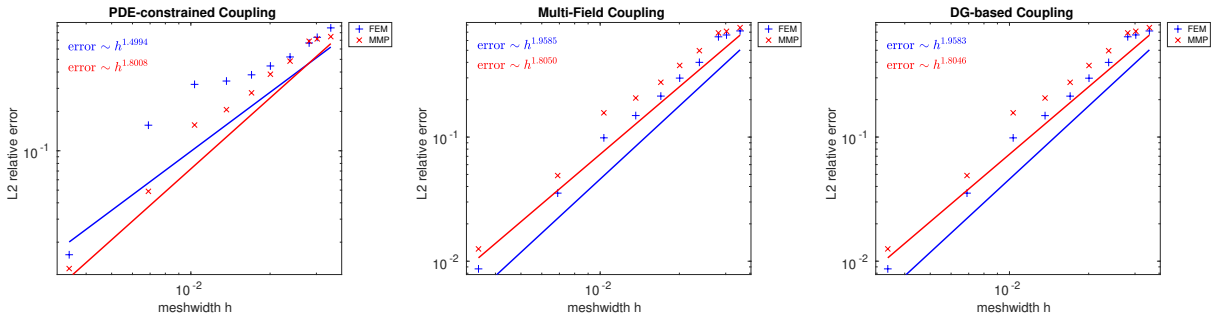


Fig. 8: h -refinement log-log error plots for 2D Helmholtz equation with exact solution. Parameters are $\epsilon_{\bullet} = 100 \epsilon_0$ and $\omega = 23.56 \cdot 10^8 \text{ rad s}^{-1}$.

4.1.1 Photonic Nanojet

Parameters $r_{\bullet} = 1 \text{ m}$, $\epsilon_{\bullet} = 2.5281 \epsilon_0$, $\mu_{\bullet} = \mu_0$, and $\omega = 23.56 \cdot 10^8 \text{ rad s}^{-1}$ permit to observe a *photonic nanojet* [14, p. 1985, Fig. 4.a] if one considers the full plane wave as excitation. This can be seen in Figure 7, which illustrates the magnitude of the *Poynting vector* [16, p. 259, (6.109)] for a simulation with the PDE-constrained least-squares coupling. The other coupling schemes yield comparable results.

4.1.2 Two MMP Domains

Parameters are still $r_{\bullet} = 1 \text{ m}$, $\epsilon_{\bullet} = 2.5281 \epsilon_0$, $\mu_{\bullet} = \mu_0$, and $\omega = 23.56 \cdot 10^8 \text{ rad s}^{-1}$. Similarly to the numerical example of Section 2.2, we split the disk Ω_{\bullet} into two halves, one modeled by FEM (Ω_f), the other by MMP (Ω_m^1): the coupling interface Γ_{f1} is therefore artificial. MMP also models the complement $\mathbb{R}^2 \setminus \Omega_{\bullet}$ (Ω_m^0): the coupling boundaries Γ_{f0} and Γ_{f1} , on the two halves of the circle, correspond to the physical discontinuity of ϵ . The geometry is shown in Figure 10a, with a sample mesh in Figure 10b.

As excitation we consider terms for $\ell = 0, \dots, 20$ from the expansion of a plane wave given by (28).

To approximate in Ω_m^1 , a single multipole expansion with Bessel functions as radial dependence is centered in the origin (Bessel functions of the first kind have no singularities in that point, which lies on $\partial\Omega_m^1$). To approximate in Ω_m^0 , a single multipole expansion with Hankel functions as radial dependence is also centered in the origin.

Figure 11 shows h -refinement convergence plots for all coupling approaches, which yield very similar results except for the multi-field coupling with λ_{01}^n discretized by $\mathcal{T}^n(\Omega_m^0)$: there is no convergence for the most refined mesh. This is because the number of degrees of freedom of $\mathcal{T}^n(\Omega_m^0)$ for that mesh is not large enough to properly impose the continuity between Ω_m^0 and Ω_m^1 .

In all the other plots we can clearly see algebraic convergence of the FEM and MMP errors with rate ~ 1.7 .

We have also considered a different configuration of multipoles. To approximate in Ω_m^1 , multipole expansions of order 1 are uniformly positioned on a circle of radius 1.5 centered in $(0.5, 0)^T$. To approximate in Ω_m^0 , multipole expansions of order 1 are uniformly positioned on a circle of radius 0.5 centered in the origin.

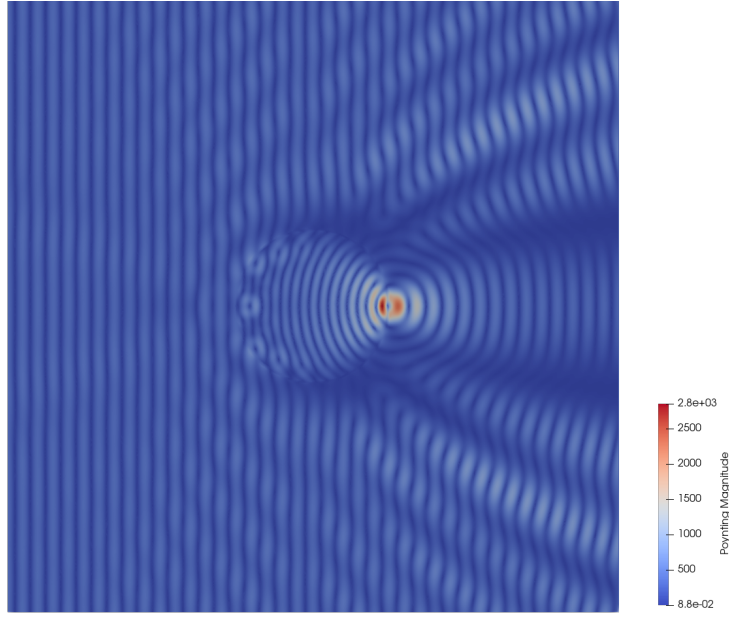


Fig. 9: Magnitude of the Poynting vector for $\epsilon_{\bullet} = 2.5281 \epsilon_0$ and $\omega = 23.56 \cdot 10^8 \text{ rad s}^{-1}$. The beam on the circumference of the disk is the photonic nanojet. Numerical solution obtained with the PDE-constrained least-squares coupling.

Figure 12 shows the corresponding h -refinement convergence plots, which look almost the same as Figure 11 but without any problem with the multi-field coupling for $\lambda_{01}^n \in \mathcal{T}^n(\Omega_m^0)$.

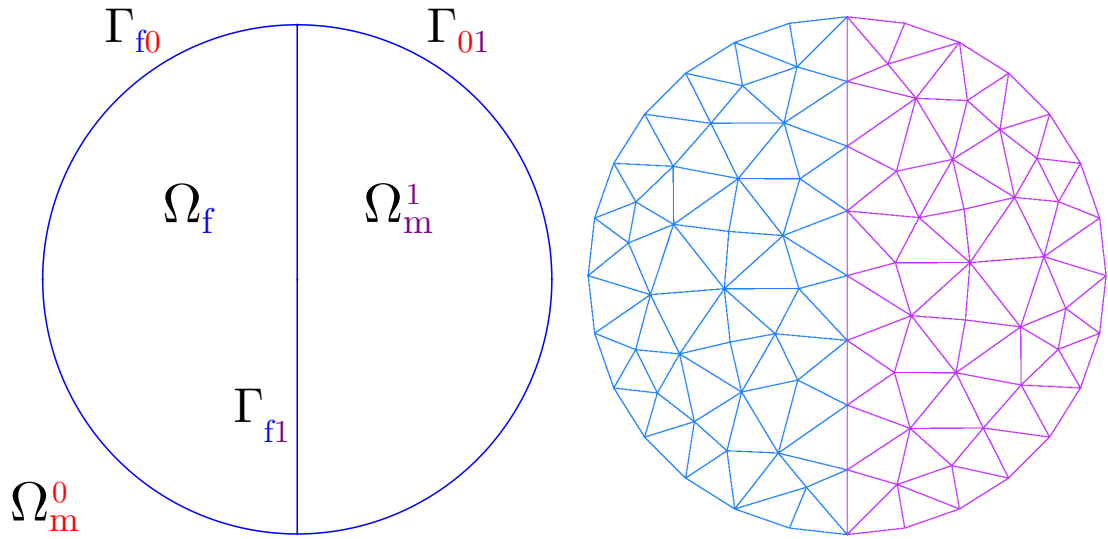
4.2 2D Scattering Problem with Triple-Point Singularities

We consider different values of ϵ in each half of the disk Ω_{\bullet} . Specifically, we take $\epsilon_+ = 4 \epsilon_0$ in the left side of Ω_{\bullet} and $\epsilon_- = 2.5281 \epsilon_0$ in the right side. ω is still $= 23.56 \cdot 10^8 \text{ rad s}^{-1}$: wavenumbers are $k_+ = 2 k_0$ and $k_- = 1.59 k_0$. Hence, at the extremes of the segment splitting Ω_{\bullet} we have triple-point singularities.

We fully surround the points with TPS by a mesh, and therefore also model with FEM a small region on the other side of the physical discontinuity of Ω_{\bullet} and an “airbox” in $\mathbb{R}^2 \setminus \Omega_{\bullet}$. The coupling interfaces Γ_{f0} and Γ_{f1} are therefore auxiliary; only the interface Γ_{01} is physical. The FEM mesh is also locally refined towards the points with TPS: the meshwidth goes like $h_0 + r^3$ (*algebraically-graded mesh*), with h_0 minimum meshwidth and r distance from the closest triple point. The geometry is shown in Figure 13a, with a sample mesh in Figure 13b.

Given the TPS, there is no exact solution: as reference we rely on the numerical solution provided by a mesh substantially more refined than the finest mesh used in the convergence study.

To approximate in Ω_m^1 , multipole expansions of order 1 with Bessel functions as radial dependence are uniformly positioned on a circle of radius 1.5 centered in $(0.5, 0)^{\top}$. To approximate in Ω_m^0 , multipole expansions of order 1 with Hankel functions as radial dependence are uniformly positioned on a circle of radius 0.5 centered in the origin.



(a) The geometry represents Ω_f , Ω_m^0 , and Ω_m^1 . The disk of radius 1 is Ω_\bullet , the area where $\epsilon \neq \epsilon_0$. The vertical segment splitting the disk in half represents the artificial coupling interface Γ_{f1} , while the two halves of the circle represent the physical coupling interfaces Γ_{f0} and Γ_{01} .

(b) 2D mesh of Ω_f and Ω_m^1 (the latter meshed for numerical quadrature of the error). The blue mesh covers Ω_f , the purple mesh Ω_m^1 .

Fig. 10: Geometry and sample mesh of the FEM domain Ω_f and the MMP domains Ω_m^0 , Ω_m^1 for simulations with exact solution.

Figure 14 shows DoF-refinement convergence plots for all coupling approaches. The PDE-constrained and DG-based coupling approaches have similar algebraic convergence patterns, but the datapoints of the multi-field coupling with multiplier $\lambda_{01}^n \in \mathcal{T}^n(\Omega_m^0)$ or $\mathcal{T}^n(\Omega_m^1)$, while they converge, are more irregular.

We repeat this experiment with the geometry shown in Figure 15a, where only the points with TPS and their immediate surrounding regions are modeled with FEM, so to minimize the meshed region. A sample mesh is shown in Figure 15b.

To approximate in Ω_m^1 and Ω_m^2 , multipole expansions of order 1 are uniformly positioned on two circles of radius 1.5 centered in $(-0.5, 0)^\top$ and $(0.5, 0)^\top$, respectively. To approximate in Ω_m^0 , multipole expansions of order 1 are uniformly positioned on a circle of radius 0.5 centered in the origin.

Figure 16 shows DoF-refinement convergence plots for the PDE-constrained and DG-based coupling approaches: we can still guess algebraic convergence.

4.3 Conclusions

Compared to other hybrid methods, such as FEM coupled with the Boundary Element Method (BEM), MMP presents the advantages of

- a simpler assembly process, as there are no singular integrals, and
- an exponentially-convergent approximation error given loose requirements on the positions of the multipoles, which can be proven rigorously for 2D Helmholtz (Section 2.2). As long as the coupling boundaries are far from sources and field singularities of the problem, the FEM–MMP coupling is also indifferent

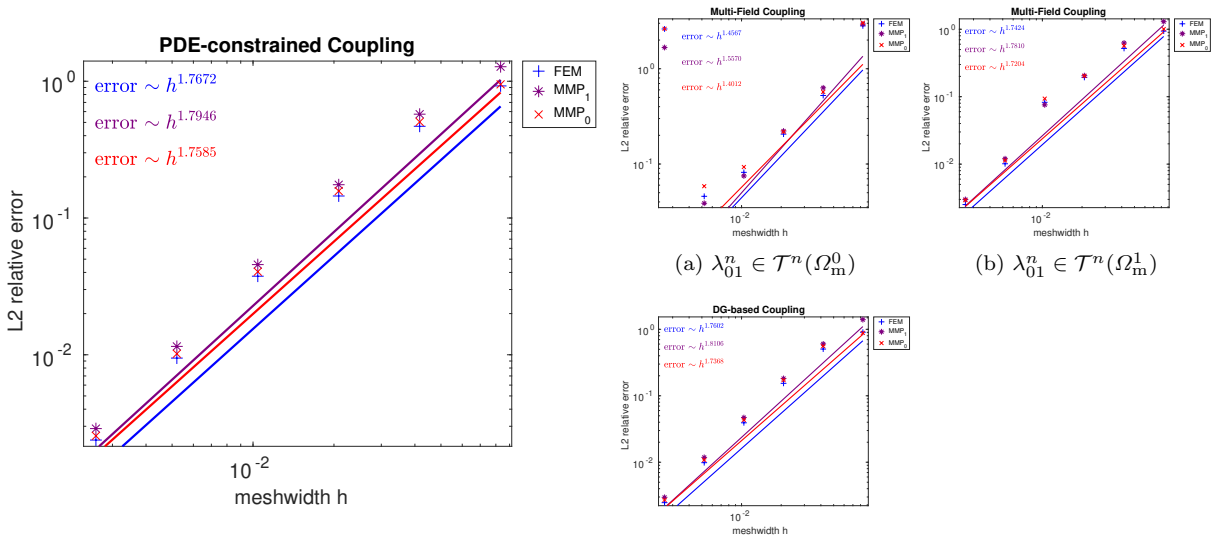


Fig. 11: h -refinement log-log error plots for 2D Helmholtz equation with exact solution solved with two MMP domains. A single multipole expansion is used for each MMP domain. Parameters are $\epsilon_\bullet = 2.5281 \epsilon_0$ and $\omega = 23.56 \cdot 10^8 \text{ rad s}^{-1}$.

towards where the multipoles are placed, and the exponential convergence of the MMP approximation error is preserved.

- Furthermore, the locally-supported piecewise-polynomial basis functions of boundary element methods [22, p. 183, Chapter 4] do not work well for high-frequency scattering problems due to the pollution effect, which is not a problem for the oscillating multipoles of MMP.

However, similarly to other hybrid methods, the FEM–MMP coupling also suffers from ill-conditioning. This is still more limited than FEM coupled with BEM due to the low number of degrees of freedom required for MMP, given its exponential convergence: the MMP dense blocks in the coupling matrices are therefore small.

Among the three coupling approaches (Sections 3.1 to 3.3), we recommend the DG-based coupling thanks to its reliability and lower number of degrees of freedom compared to the PDE-constrained coupling. The multi-field coupling has a similar amount of degrees of freedom to the DG-based one, but can have stability issues caused by the nonconforming discretization of its Lagrange multipliers.

A future paper will present the FEM–MMP coupling with multiple MMP domains applied to vector scattering problems in \mathbb{R}^3 (time-harmonic Maxwell’s equations).

References

1. Arnold, D.N., Brezzi, F., Cockburn, B., Marini, L.D.: Unified analysis of Discontinuous Galerkin methods for elliptic problems. *SIAM Journal on Numerical Analysis* **39**(5), 1749–1779 (2002). DOI 10.1137/S0036142901384162
2. Babuška, I.M., Sauter, S.A.: Is the pollution effect of the FEM avoidable for the Helmholtz equation considering high wave numbers? *SIAM Review* **42**(3), 451–484 (2000). DOI 10.2307/2653302
3. Barnett, A.H., Betcke, T.: An exponentially convergent nonpolynomial finite element method for time-harmonic scattering from polygons. *SIAM Journal on Scientific Computing* **32**(3), 1417–1441 (2010). DOI 10.1137/090768667
4. Bohren, C.F., Huffman, D.R.: Absorption and scattering of light by small particles. Wiley (2007). DOI 10.1002/9783527618156

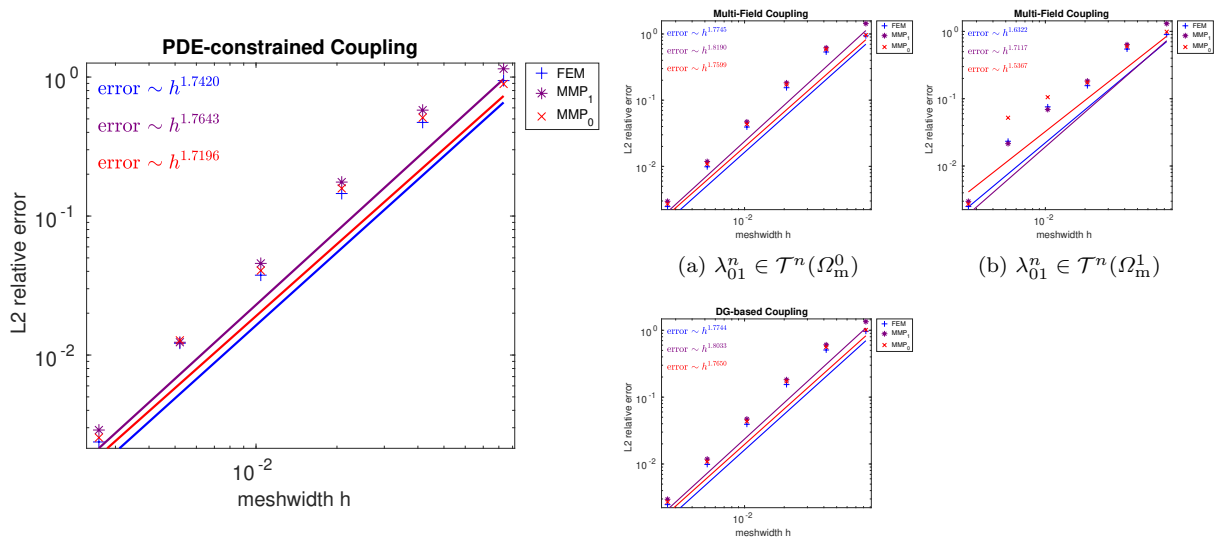
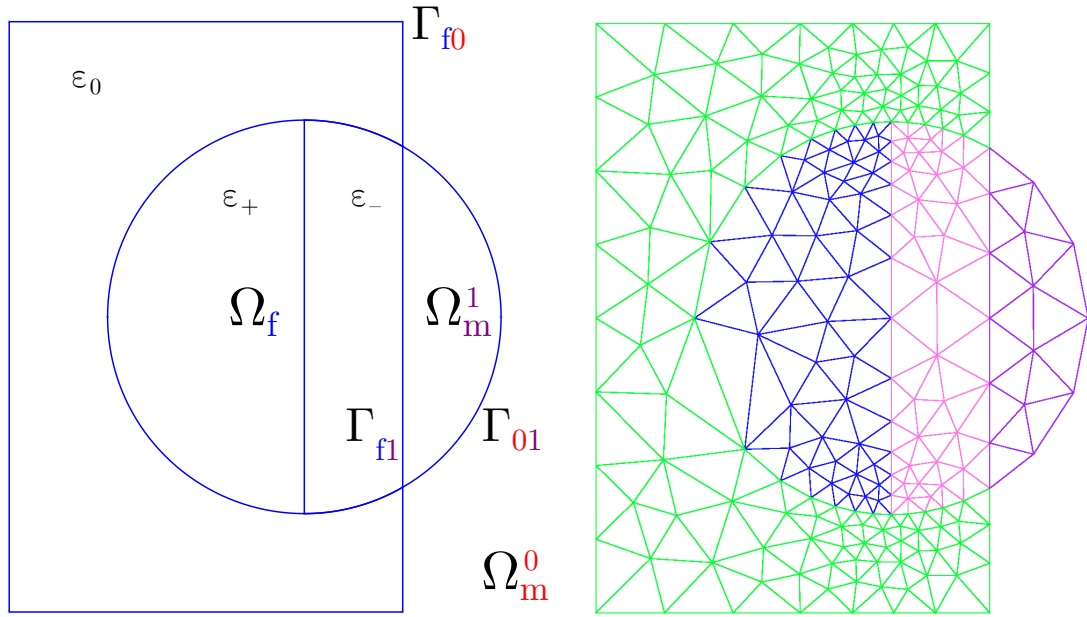


Fig. 12: h -refinement log-log error plots for 2D Helmholtz equation with exact solution solved with two MMP domains. Many multipole expansions on circles are used for each MMP domain. Parameters are $\epsilon_{\bullet} = 2.5281 \epsilon_0$ and $\omega = 23.56 \cdot 10^8 \text{ rad s}^{-1}$.

5. Brezzi, F., Marini, L.D.: A three-field domain decomposition method. In: Domain decomposition methods in science and engineering (Como, 1992), *Contemp. Math.*, vol. 157, pp. 27–34. Amer. Math. Soc., Providence, RI (1994). DOI 10.1090/conm/157/01402
6. Casagrande, R., Winkelmann, C.: Hybrid Discontinuous finite elements for power devices (HyDi) (2016). ABB Corporate Research Center
7. Casati, D., Hiptmair, R.: Coupling finite elements and auxiliary sources. *Computers & Mathematics with Applications* **77**(6), 1513–1526 (2019). DOI 10.1016/j.camwa.2018.09.007
8. Casati, D., Hiptmair, R., Smajic, J.: Coupling finite elements and auxiliary sources for Maxwell’s equations. *International Journal of Numerical Modelling: Electronic Networks, Devices and Fields* (forthcoming). DOI 10.1002/jnm.2534
9. Colton, D., Kress, R.: Inverse acoustic and electromagnetic scattering theory, *Applied Mathematical Sciences*, vol. 93, 3rd edn. Springer, Heidelberg (2013)
10. Geuzaine, C., Remacle, J.F., et al.: Gmsh v4.1.4 (2019). <http://gmsh.info/>
11. Greengard, L., Lee, J.Y.: Stable and accurate integral equation methods for scattering problems with multiple material interfaces in two dimensions. *J. Comput. Phys.* **231**, 2389–2395 (2012). DOI 10.1016/j.jcp.2011.11.034
12. Guennebaud, G., Jacob, B., et al.: Eigen v3.3.7 (2018). <http://eigen.tuxfamily.org>
13. Hafner, C.: Beiträge zur Berechnung der Ausbreitung elektromagnetischer Wellen in zylindrischen Strukturen mit Hilfe des “Point-Matching”-Verfahrens (1980)
14. Heifetz, A., Kong, S.C., Sahakian, A.V., Taflove, A., Backman, V.: Photonic nanojets. *Journal of Computational and Theoretical Nanoscience* **6**(9), 1979–1992 (2009). DOI 10.1166/jctn.2009.1254
15. Hiptmair, R., Moiola, A., Perugia, I.: A survey of Trefftz methods for the Helmholtz equation, pp. 237–279. Springer, Cham (2016). DOI 10.1007/978-3-319-41640-3_8
16. Jackson, J.D.: Classical electrodynamics, 3rd edn. Wiley, New York, NY (1999)
17. McLean, W.: Strongly elliptic systems and boundary integral equations. Cambridge University Press, Cambridge (2000)
18. Mie, G.: Elektrische Wellen an zwei parallelen Drähten. *Annalen der Physik* **307**, 201–249 (1900). DOI 10.1002/andp.19003070602
19. Moiola, A.: Trefftz-Discontinuous Galerkin methods for time-harmonic Galerkin methods for time-harmonic wave problems. PhD thesis, Seminar for Applied Mathematics, ETH Zurich (2011). DOI 10.3929/ethz-a-006698757
20. Monk, P.: Finite element methods for Maxwell’s equations. Clarendon Press, Oxford (2003). DOI 10.1093/acprof:oso/9780198508885.001.0001
21. Popp, A., Wohlmuth, B.I., Gee, M.W., Wall, W.A.: Dual quadratic mortar finite element methods for 3D finite deformation contact. *SIAM Journal on Scientific Computing* **34**(4), B421–B446 (2012). DOI 10.1137/110848190



(a) The geometry represents Ω_f , Ω_m^0 , and Ω_m^1 . The disk of radius 1 is Ω_\bullet : in one half, $\epsilon = \epsilon_+$; in the other, $\epsilon = \epsilon_-$. In the rectangle outside the disk, $\epsilon = \epsilon_0$.

(b) 2D mesh of Ω_f and Ω_m^1 (the latter meshed for numerical quadrature of the error). The blue, pink, and green meshes cover Ω_f and are characterized by parameters ϵ_+ , ϵ_- , and ϵ_0 , respectively. The purple mesh covers Ω_m^1 and is characterized by ϵ_- .

Fig. 13: Geometry and sample mesh of the FEM domain Ω_f and the MMP domains Ω_m^0 , Ω_m^1 for simulations with triple-point singularities.

22. Sauter, S.A., Schwab, C.: Boundary element methods, *Springer Series in Computational Mathematics*, vol. 39. Springer, Berlin, Heidelberg (2011). DOI 10.1007/978-3-540-68093-2
23. Schenk, O., et al.: PARDISO v6.0 (2018). <https://www.pardiso-project.org/>
24. Smajic, J., Hafner, C., Leuthold, J.: Coupled FEM–MMP for computational electromagnetics. *IEEE Transactions on Magnetics* **52**(3), 1–4 (2015). DOI 10.1109/TMAG.2015.2475241
25. Stenberg, R.: Mortaring by a method of J.A. Nitsche. *Computational Mechanics: new trends and applications* (1998)
26. Süli, E., Schwab, C., Houston, P.: hp-DGFEM for partial differential equations with nonnegative characteristic form. In: B. Cockburn, G.E. Karniadakis, C.W. Shu (eds.) *Discontinuous Galerkin methods, Lecture Notes in Computational Science and Engineering*, vol. 11, pp. 221–230. Springer, Berlin, Heidelberg (2000)
27. Vekua, I.N.: *New methods for solving elliptic equations*. North Holland Publishing Company (1967)

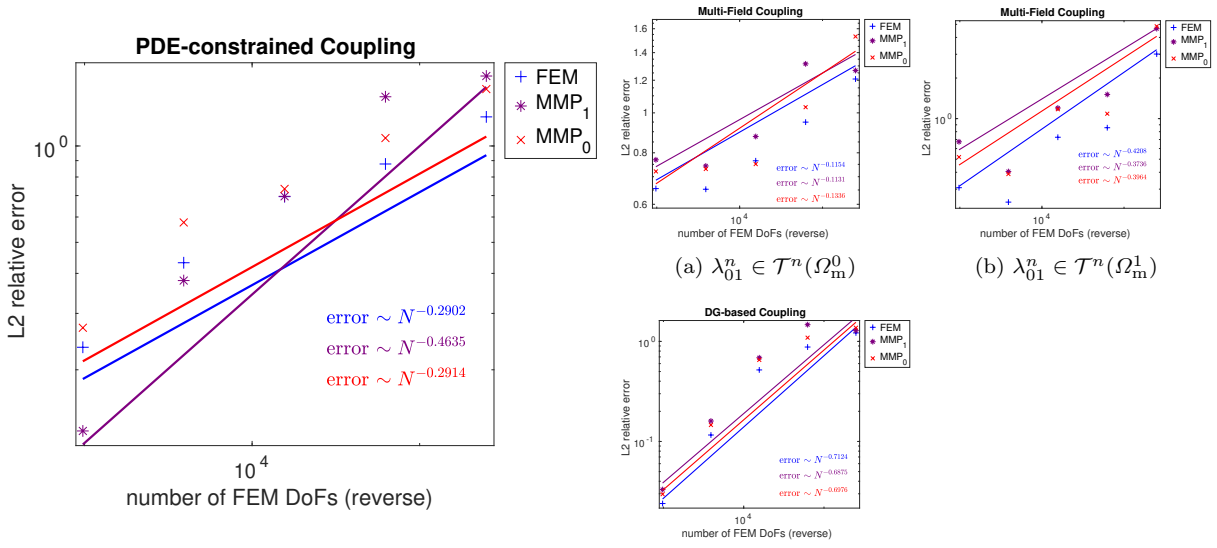
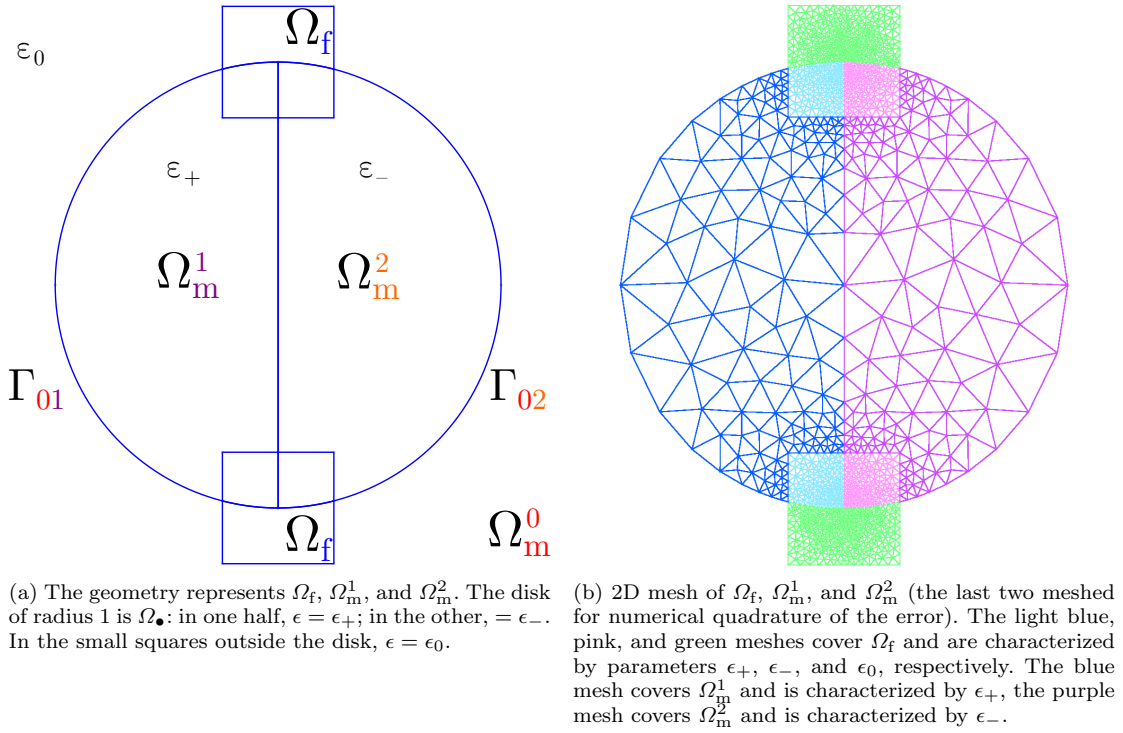


Fig. 14: DoF-refinement log-log error plots for 2D Helmholtz equation with TPS solved with two MMP domains (geometry in Figure 13a). Parameters are $\epsilon_+ = 4\epsilon_0$, $\epsilon_- = 2.5281\epsilon_0$, and $\omega = 23.56 \cdot 10^8 \text{ rad s}^{-1}$.



(a) The geometry represents Ω_f , Ω_m^1 , and Ω_m^2 . The disk of radius 1 is Ω_\bullet : in one half, $\epsilon = \epsilon_+$; in the other, $\epsilon = \epsilon_-$. In the small squares outside the disk, $\epsilon = \epsilon_0$.

(b) 2D mesh of Ω_f , Ω_m^1 , and Ω_m^2 (the last two meshed for numerical quadrature of the error). The light blue, pink, and green meshes cover Ω_f and are characterized by parameters ϵ_+ , ϵ_- , and ϵ_0 , respectively. The blue mesh covers Ω_m^1 and is characterized by ϵ_+ , the purple mesh covers Ω_m^2 and is characterized by ϵ_- .

Fig. 15: Geometry and sample mesh of the FEM domain Ω_f and the (bounded) MMP domains Ω_m^1 and Ω_m^2 for simulations with triple-point singularities.

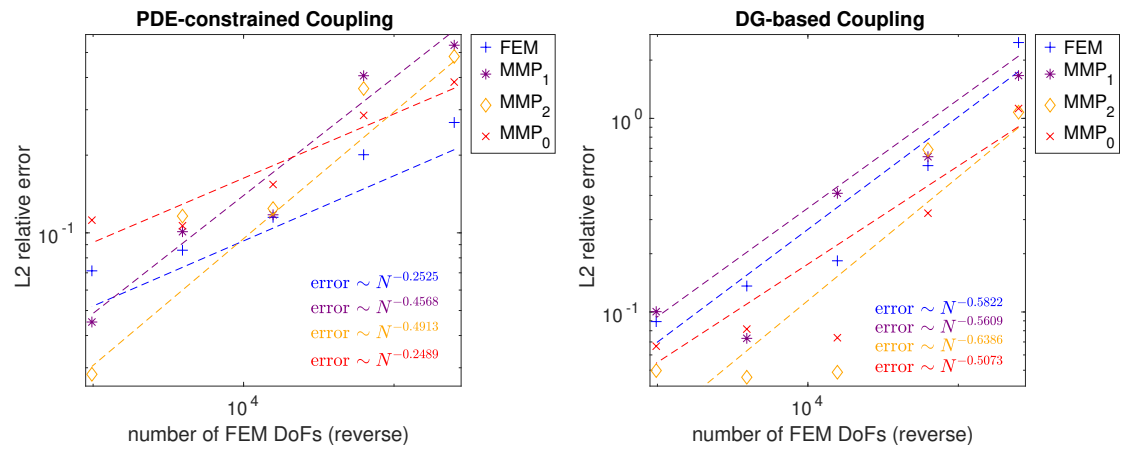


Fig. 16: DoF-refinement log-log error plots for 2D Helmholtz equation with TPS solved with three MMP domains (geometry in Figure 15a). Parameters are $\epsilon_+ = 4\epsilon_0$, $\epsilon_- = 2.5281\epsilon_0$, and $\omega = 23.56 \cdot 10^8 \text{ rad s}^{-1}$.